

**Kinematic and mechanical response of dry woven fabrics in through-thickness compression**

**Virtual fiber modeling with mesh overlay technique and experimental validation**

Daelemans, Lode; Tomme, Brecht; Caglar, Baris; Michaud, Véronique; Van Stappen, Jeroen; Cnudde, Veerle; Boone, Matthieu; Van Paepegem, Wim

**DOI**

[10.1016/j.compscitech.2021.108706](https://doi.org/10.1016/j.compscitech.2021.108706)

**Publication date**

2021

**Document Version**

Accepted author manuscript

**Published in**

Composites Science and Technology

**Citation (APA)**

Daelemans, L., Tomme, B., Caglar, B., Michaud, V., Van Stappen, J., Cnudde, V., Boone, M., & Van Paepegem, W. (2021). Kinematic and mechanical response of dry woven fabrics in through-thickness compression: Virtual fiber modeling with mesh overlay technique and experimental validation. *Composites Science and Technology*, 207, Article 108706. <https://doi.org/10.1016/j.compscitech.2021.108706>

**Important note**

To cite this publication, please use the final published version (if applicable).  
Please check the document version above.

**Copyright**

Other than for strictly personal use, it is not permitted to download, forward or distribute the text or part of it, without the consent of the author(s) and/or copyright holder(s), unless the work is under an open content license such as Creative Commons.

**Takedown policy**

Please contact us and provide details if you believe this document breaches copyrights.  
We will remove access to the work immediately and investigate your claim.

1 <https://doi.org/10.1016/j.compscitech.2021.108706>

2  
3 **Kinematic and mechanical response of dry woven fabrics in through-thickness**  
4 **compression: virtual fiber modeling with mesh overlay technique and**  
5 **experimental validation**

6 *Lode Daelemans<sup>1\*</sup>, Brecht Tomme<sup>1</sup>, Baris Caglar<sup>2,3</sup>, Véronique Michaud<sup>2</sup>, Jeroen Van Stappen<sup>4,5</sup>, Veerle*  
7 *Cnudde<sup>4,5,6</sup>, Matthieu Boone<sup>4,7</sup>, Wim Van Paepegem<sup>1</sup>*

8 <sup>1</sup> *Department of Materials, Textiles and Chemical Engineering (MATCH), Ghent University, Technologiepark 70A,*  
9 *B-9052 Zwijnaarde, Belgium*

10 <sup>2</sup> *Laboratory for Processing of Advanced Composites (LPAC), Institute of Materials (IMX), Ecole Polytechnique*  
11 *Fédérale de Lausanne (EPFL), Station 12, Lausanne CH-1015, Switzerland*

12 <sup>3</sup> *Aerospace Manufacturing Technologies, Faculty of Aerospace Engineering, Delft University of Technology,*  
13 *Kluyverweg 1, Delft 2629HS, the Netherlands*

14 <sup>4</sup> *Centre for X-ray Tomography (UGCT), Ghent University, Proeftuinstraat 86, B-9000 Ghent, Belgium*

15 <sup>5</sup> *Department of Geology, Pore-Scale Processes in Geomaterials Research (PProGRess), Ghent University,*  
16 *Krijgslaan 281/S8, B-9000 Ghent, Belgium*

17 <sup>6</sup> *Environmental Hydrogeology, Department of Earth Sciences, Utrecht University, Princetonlaan 8a, 3584 CB*  
18 *Utrecht, The Netherlands*

19 <sup>7</sup> *Department of Physics and Astronomy, Radiation Physics - UGCT, Ghent University, Proeftuinstraat 86, B-9000*  
20 *Ghent, Belgium*

21 *\* [Lode.Daelemans@UGent.be](mailto:Lode.Daelemans@UGent.be)*

---

22 **Abstract**

23 The through-thickness compressive behavior of fabric reinforcements is crucial in liquid  
24 composite molding manufacturing processes. Predictive simulations of the compressive  
25 response are thus necessary to enable a virtual processing workflow. These are complex  
26 however, as the compressive behavior of the reinforcement fabrics is non-linear. Although  
27 virtual fiber modeling has proven to be a strong kinematical tool, it cannot predict the  
28 compressive response due to the lack of bending stiffness in the virtual fibers. Here, we  
29 describe a solution that enables predictive compressive simulations through hybrid virtual  
30 fibers. It is based on an overlay mesh-element technique, combining both (i) finite  
31 elements that determine the in-plane fiber properties as well as (ii) finite elements that  
32 determine out-of-plane fiber bending. Using these hybrid virtual fibers, the through-  
33 thickness compression of a twill woven fabric ply is simulated and experimentally  
34 validated using both  $\mu$ CT-based as compliance-based measurements. Excellent  
35 agreement between simulation and experiment is obtained for the right set of input  
36 parameters.

37 **Keywords:** A. Fabrics/textiles, B. Mechanical properties, C. Finite element analysis  
38 (FEA), D. X-ray computed tomography, Digital element analysis

---

## 39 **1. Introduction**

40 Liquid Composite Molding (LCM) processes such as Vacuum Assisted Resin Transfer  
41 Molding (VARTM), Resin Transfer Molding (RTM), or Injection Compression Molding  
42 (ICM), are composite manufacturing processes in which a dry fibrous reinforcement is  
43 infused with liquid resin. The permeability of the fibrous reinforcement is key to allow  
44 sufficient flow of resin throughout the reinforcement, resulting in high-quality parts that  
45 are used in industry, for example in the automotive, marine, and civil sectors. The flow is  
46 usually dual-scaled, with micro-porous channels between reinforcing fibers, and meso-  
47 porous channels dependent on the reinforcement textile structure each affecting the flow  
48 [1]. Moreover, the reinforcement is compressed between two mold halves in LCM  
49 processes and its microstructure hence changes because of the applied pressure (e.g. tow  
50 compaction). Hence, understanding and predicting the through-thickness compression  
51 behavior of reinforcements is one of the crucial factors in the manufacturing of high-  
52 quality composite parts through LCM processes.

53 A large body of research is devoted to experimental analysis of the through-thickness  
54 compression of fabrics and typically relies on extensive high-resolution X-ray micro-  
55 computed tomography ( $\mu$ CT) analysis to determine the structure of reinforcement textiles  
56 under pressure [1–8]. Although modeling techniques would provide a good alternative,  
57 the fibrous nature of textile reinforcements complicates out-of-plane properties such as  
58 through-thickness compression due to dominant deformation mechanisms on the  
59 microscale such as fiber realignment. Although macro- and mesoscale models exist, these  
60 are usually fitted with specific constitutive laws based on experimentally determined  
61 through-thickness input properties [9]. In addition, they do not reveal conclusions about  
62 the micro-level which would be relevant for microscale permeability.

63 Microscale models offer the possibility to analyze the through-thickness compression at  
64 the reinforcement level while taking into account the microscale deformation  
65 mechanisms. Most notably, the virtual fiber modeling method, initially conceived by  
66 Wang *et al.* [10,11], is proving to be one of the most viable options. Often referred to as  
67 the digital element method, this method is centered around the modeling of fibers through  
68 a chain of truss-like elements (digital elements), simulating the textile material as made  
69 up of a relatively small amount of such “virtual” fibers (up to 100-200). The virtual fiber

70 method thus explicitly takes into account the fibrous behavior of the reinforcements at  
71 near-microscale.

72 Recently, multiple researchers have shown that the virtual fiber modeling of textile  
73 reinforcements captures relevant deformation mechanisms such as the yarn cross-  
74 sectional deformation and yarn path waviness and that the predicted microstructures  
75 correlate well to those observed by  $\mu$ CT imaging [12–17]. Yet, the kinematic nature of  
76 the simulations limits their ability to link the mechanics with the kinematics, e.g. to  
77 simulate pressure-dependent microstructure. This is especially true in the case of out-of-  
78 plane loadings such as compression, where the reinforcement response is dominated by  
79 fiber bending and by creation of new contact surfaces due to fiber realignment. In the case  
80 of in-plane loadings, the response is dominated by tensile loading in the fiber directions  
81 and we have previously reported a successful correlation between kinematics and  
82 mechanics for these cases [18,19]. The virtual fiber modeling method has recently been  
83 applied to through-thickness compression of woven fabrics with successful validation of  
84 the microstructure (e.g. yarn compaction, yarn paths, ...) to experimental data [20,21].  
85 Yet in both cases, the modeling is kinematic only in that the compaction in the models is  
86 realized without taking the actual pressure level into account. Although this enables  
87 meso-scale models to include the correct mechanical behavior by using the predicted  
88 microstructures [21], virtual fiber modeling with correct out-of-plane mechanics might  
89 provide a more efficient route for virtual mechanical analysis of textile reinforcements.

90 The benefits of the virtual fiber modeling approach over the wider used meso-scale  
91 approach, e.g. [9,22,23], can be summarized as:

92 (i) The initial yarn shape and configuration in the textile fabric can be simulated, and thus  
93 does not require any a priori shape assumptions (e.g. elliptical, lenticular, ... cross-  
94 sections) nor dedicated geometry extraction from microscopic images (e.g. micro-  
95 computed tomography).

96 (ii) The transversal behavior related to the realignment of fibers within the yarn under  
97 load is naturally implemented without requiring dedicated material constitutive laws. In  
98 essence, this enables to directly take into account yarn specific properties, for example,  
99 yarn twist or the use of multiple fiber types within a yarn, instead of recalibrating the  
100 constitutive laws. Moreover, there is also an option to use a virtual fiber modeling  
101 approach to determine the input properties for mesoscopic and macroscopic models, e.g.

102 such as developed in Refs. [22,24,25], creating a stronger virtual textile modeling  
103 workflow.

104 (iii) The discrete nature of the yarn consisting out of many fibers offers more deformation  
105 modes. In comparison, meso-scale models could run into problems under severe yarn  
106 deformations where the continuum approach does not suffice, e.g. where yarns would  
107 flatten out, unravel or split. Such loadings can be encountered for example in process  
108 modeling where the yarns come into contact with surfaces or tools (e.g. tufting needles,  
109 mold surfaces, sharp corners, ...).

110 These advantages make that the virtual fiber modeling approach has its benefits to co-  
111 exist alongside meso-scale modeling, where it allows an additional level of detail situated  
112 between the micro- and the meso-scale.

113 In this paper, we describe a framework to enable the correct inclusion of fiber bending  
114 into the virtual fiber modeling approach, to predict the through-thickness compression of  
115 a twill woven glass fibre fabric reinforcement. It is based on an overlay mesh-element  
116 technique, combining both (i) finite elements that determine the in-plane fiber properties  
117 as well as (ii) finite elements that determine out-of-plane fiber bending. This method is  
118 applied to the through-thickness compression of a single layer of dry fabric reinforcement  
119 to exclude any effects by the nesting of multiple layers. To validate the model, two  
120 different test methods are used to determine the pressure-compaction relationship for a  
121 single reinforcement ply with adequate resolution.

## 122 **2. Simulation details**

### 123 ***2.1. Generation of an as-woven state***

124 Starting from an idealized unit cell geometry, the as-woven state of the twill fabric is  
125 generated using the virtual fiber principle as reported for example in our earlier work for  
126 3D woven fabrics within the Abaqus 2019 Finite Element Analysis environment [18]  
127 (**Figure 1**). Briefly, an idealized and “loose” unit cell geometry, based on the values  
128 reported in **Table 1**, is created. A shrinkage step then creates tensile forces in the yarns  
129 similar to those present in an actual weaving step. By tensioning the yarns, the fibers will  
130 realign and spread out, creating the typical lenticular yarn cross-sectional shapes. This  
131 results in the as-woven state of the fabric. Periodicity of the unit cell is ensured using  
132 periodic boundary conditions proposed by Green *et al.* [15] and Thompson *et al.* [21],

133 consisting of periodicity imposed at individual fiber ends as well as slave yarns that  
134 provide a contact surface at the unit cell edges.

135 Here, the virtual fibers consist of chains of linear elastic truss elements (T3D2 elements,  
136 Abaqus/Explicit) with properties representing glass fiber properties. All input properties  
137 that are used are related to actual physical and measurable parameters (see Table 1). Note  
138 that the majority of these parameters can already be found in the datasheets of the fiber  
139 and fabric material, making extended experimental characterization unnecessary.

140 The diameter of the virtual fibers  $D_{vf}$  (circular cross-section) is chosen such that the  
141 physical cross-sectional area of the virtual and real yarn,  $A_{vy}$  and  $A_{ry}$  are equal:

$$A_{vy} = n_{vf} \frac{\pi}{4} D_{vf}^2 = A_{ry} = n_{rf} \frac{\pi}{4} D_{rf}^2 \rightarrow D_{vf} \quad (1)$$

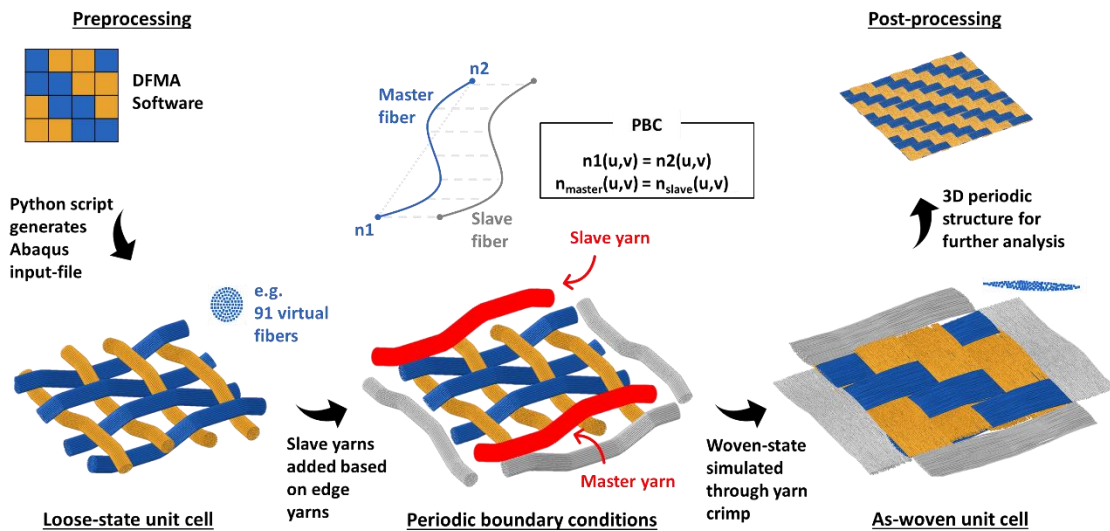
142 where  $n_{vf}$  and  $n_{rf}$  are the number of fibers in the virtual and in the real yarn, and,  $D_{rf}$  is  
143 the diameter of the fibers in the real yarn (which can be measured, or calculated from the  
144 tex-value of the fibers if the density is known).

145 Since the cross-sectional area is equal, volumetric properties such as the Young's  
146 modulus or tensile strength of the real fibers can be assigned to the virtual fibers as well.  
147 Surface properties, such as frictional constants, however, will be affected by the  
148 discretization of the yarns into a relatively low amount of virtual fibers (30 – 130,  
149 compared to the thousands of fibers in an actual yarn). The yarn-to-yarn friction for glass  
150 fiber yarns is reported to vary between 0.2 – 0.4 depending on the tension and normal  
151 pressure applied to the yarns, their velocity (static versus dynamic friction), and the  
152 sliding directions (parallel or transverse to each other) [26]. Generally, lower friction  
153 coefficients are found at higher velocities and forces, such as may be encountered during  
154 weaving. Therefore, it was decided to impose a friction coefficient of 0.2 in our as-woven  
155 simulations. Contacts are handled by the *General Contact* algorithm in Abaqus between  
156 the fiber surfaces. The final as-woven state is reached by imposing a shrinkage factor on  
157 the yarns in the “loose-state” such that the final crimp of the yarns is equal to the  
158 experimentally determined crimp.

159 The idealized unit cell geometry is created through the Dynamic Fabric Mechanical  
160 Analyzer (DFMA, [www.fabricmechanics.com](http://www.fabricmechanics.com)) from the Fabric Mechanics group at  
161 Kansas State University (Wang *et al.*), who originally published the virtual fiber principle  
162 in Refs. [10,11]. Although the software itself is capable of mechanical analysis, the

163 simulations in this work are performed using the finite element analysis package Abaqus  
 164 as it allows the use of an explicit solver, a mesh overlay technique (see Section 2.2) and  
 165 more complex boundary and contact conditions. The DFMA software was thus used here  
 166 only as a pre-processor; the idealized geometry is generated in DFMA and then exported  
 167 through a dedicated python script to an Abaqus 2019 input file for the as-woven  
 168 simulation.

169 The initial loose-state unit cell consists of fibers and yarns in a curved position. As such,  
 170 truss element based virtual fibers (which have no bending stiffness) are perfectly suited.  
 171 In fact, implementation of bending stiffness at this step would only result in spurious  
 172 stresses as the virtual fibers would want to relax back to their initial, and thus curved,  
 173 positions. In reality, yarns entering a weaving loom are straight instead of curved and are  
 174 subsequently deformed to form the as-woven state.



175

176 **Figure 1** – Conceptual overview of the as-woven fabric generation using the virtual fiber principle and periodic  
 177 boundary conditions.

178

179 **2.2. Overlay mesh technique and compression simulation**

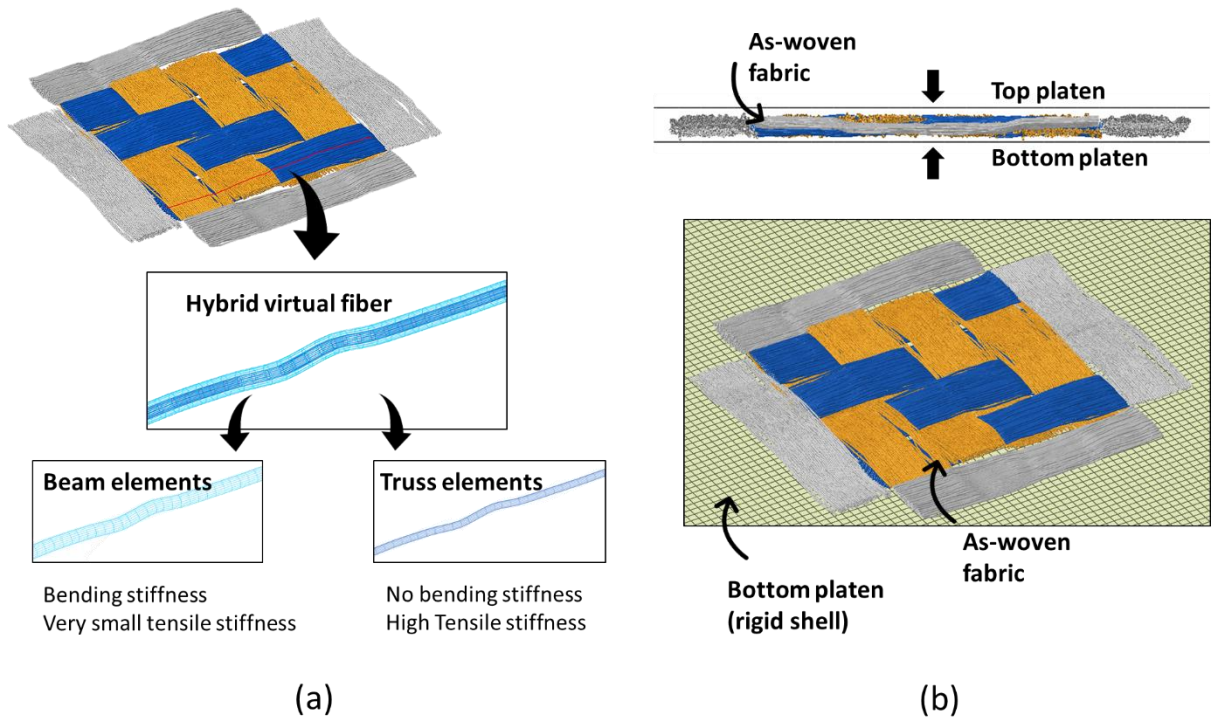
180 Bending stiffness is imposed on the virtual fibers by overlaying the truss elements with  
 181 beam elements (B31, Abaqus/Explicit) using the same nodes, see **Figure 2a**. This creates  
 182 hybrid virtual fibers in which the truss elements will determine the properties in the fiber  
 183 direction (tensile stiffness), while the beam elements are chosen such that they do not  
 184 affect those properties (negligible Young’s modulus), but have a certain bending stiffness  
 185  $EI$ . The value of that bending stiffness can be set to the required value by changing either

186 the Young's modulus  $E$  or the beam element radius which defines its second moment of  
187 inertia  $I (= \pi r^4)$ . Here we opted to fix the Young's modulus such that  $E_{truss} =$   
188  $100 E_{beam}$  to suppress any effects that might rise from the stiffness of the beam elements.  
189 For the range of  $EI$  considered, the beam radius was similar to that of the truss elements,  
190 ensuring that the overall tensile stiffness of the virtual fibers was barely affected by the  
191 superimposed beam elements. The virtual fiber bending stiffness was set as follows:

$$n_{vf} E_{beam} I_{vf,beam} = (EI)_{measured} \quad (2)$$

192 The through-thickness compression is simulated by two rigid platens (rigid shell elements  
193 R3D4, Abaqus/Explicit) which move towards each other (displacement-controlled) with  
194 the fabric reinforcement in between, see **Figure 2b**. The simulation is performed under  
195 quasi-static conditions in Abaqus 2019 Explicit (the internal energy is much higher than  
196 the kinetic energy). Contact between the virtual fiber surfaces and their surroundings  
197 (other fibers and compression platens) is imposed on the truss elements only and is  
198 defined by Abaqus' *General Contact* algorithm. The beam elements are excluded from  
199 any contact definition as their radius is dependent on the required bending stiffness and  
200 does not represent the fiber radius, the fiber radius is equal to the truss element radius.  
201 During compression of the as-woven fabric, the reaction forces on the platens and the  
202 distance between them are used to determine the pressure-thickness and pressure-volume  
203 fraction curves. The same periodic boundary conditions as before are used.





204

205 **Figure 2** – (a) The fabric is constructed of hybrid virtual fibers that consist of a chain of beam elements for bending  
 206 stiffness and truss element for tensile stiffness. (b) Overview of the through-thickness compression setup (for clarity  
 207 the top platen is hidden in the overview image).

208 **3. Experimental details**

209 **3.1. Fiber, yarn and fabric properties**

210 Table 1 gives an overview of all the properties of the dry glass fiber twill fabric (Interglas  
 211 92140 aero, finish FK 144, 2x2 twill woven, 390 g/m<sup>2</sup>, purchased through R&G  
 212 Faserverbundwerkstoffe GmbH, Waldenbuch, Germany) that serve as input for the  
 213 simulations. Several properties are measured experimentally, instead of relying on  
 214 averaged datasheet values, to achieve higher accuracy of the simulations. Note that the  
 215 majority of the required input properties are usually given in the datasheet of the fabric  
 216 and fiber material, or are relatively easy to determine/calculate. Only the bending stiffness  
 217 of the yarns is usually not given and has to be measured for example by Peirce’s cantilever  
 218 method. This method is relatively simple and barely requires any investment in  
 219 machinery.

220 **Table 1** – Input properties used in the simulations obtained from measurements, calculations, or datasheet values.  
 221 Values between brackets are datasheet values.

Property	Warp	Weft	Property determination
<b>FIBERS</b>			

Linear density (dTex)	1.57		Measured according to ISO 1973 (vibroscope)
Average fiber diameter ( $\mu\text{m}$ )	8.9 (9)		Calculated from linear density and volumetric density.
Volumetric density ( $\text{kg m}^{-3}$ )	(2550)		Datasheet value.
E-modulus (cN/dTex   GPa)	292   74.6		Measured according to ASTM D3822.
<b>YARNS</b>			
Linear density (Tex)	338 (340)	269 (272)	Measured according to ISO 7211-5.
Fibers per yarn (-)	2148	1708	Calculated from linear densities of yarn and fiber.
Bending stiffness ( $10^{-7}$ Nm <sup>2</sup> )	1.49	0.99	Measured according to ASTM D1388.
<b>FABRIC</b>			
Areal density ( $\text{g m}^{-2}$ )	387 (390)		Measured.
Thread count ( $\text{cm}^{-1}$ )	6.1 (6.0)	6.5 (6.7)	Measured according to ISO 7211-2.
Yarn spacing (cm)	0.164	0.154	Calculated from thread count.
Crimp (%)	0.55	0.75	Measured according to ISO 7211-3.

222

### 223 **3.2. Through-thickness compression testing**

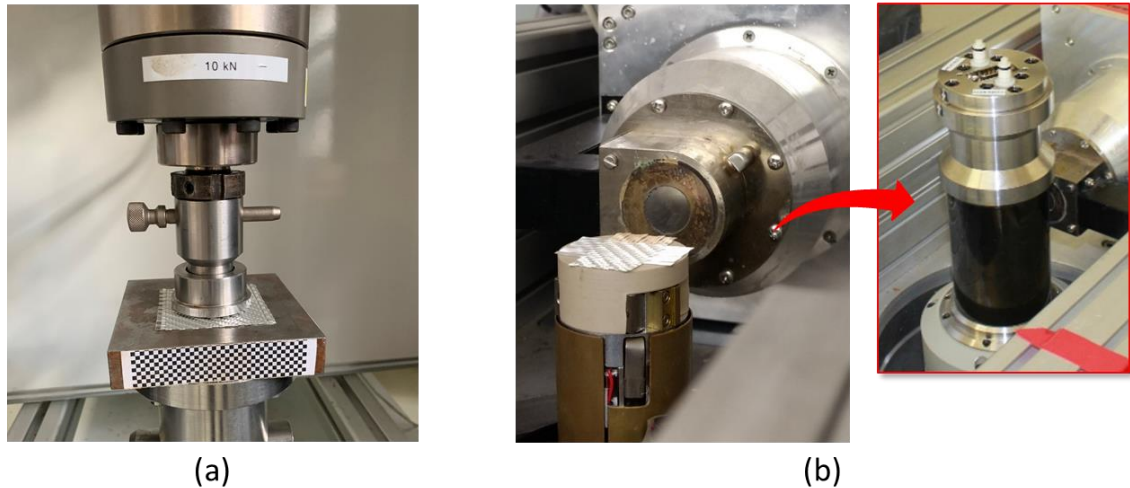
224 We opted for two different ways to measure the through-thickness compressive response  
225 of a single fabric layer due to the difficulty in achieving the required platen-to-platen  
226 distance accurately enough: (i) using a compliance-calibration and self-aligning  
227 compression setup (setup 1, **Figure 3a**, available at Ecole Polytechnique Fédérale de  
228 Lausanne), and, (ii) using in-situ X-ray micro-computed tomography ( $\mu\text{CT}$ ) with a  
229 dedicated compression cell that allows imaging of specimens during mechanical loading  
230 (setup 2, **Figure 3b**, available at Ghent University).

231 Setup 1 consists of two steel platens, the lower one a square surface of 100 mm x 100 mm  
232 and connected to a universal testing machine (Walter + Bai LFM-125kN equipped with  
233 a 10kN load cell) with a fixed support [27]. The upper platen has a circular surface with  
234 a diameter of 45 mm and contains a ball-pivot system for self-alignment that maintains  
235 parallelism between the lower and upper platens. A single layer of fabric cut to  
236 dimensions of 60 mm x 60 mm was compressed between the platens. Each compression

237 measurement on this setup is preceded by a measurement without a specimen. The  
238 calibration curve obtained in the measurement without a specimen is used for compliance  
239 correction of the following compression measurement. Compliance correction is  
240 performed, for all recorded force values in the compression test, by subtracting the  
241 corresponding thickness in the compliance test from the thickness in the compression test  
242 [28].

243 Setup 2 consists of two machined poly-ether-ether-ketone (PEEK) compression platens  
244 that are attached to an in-situ mechanical stage (CT5000, Deben, Suffol, United  
245 Kingdom) in combination with an internal load cell of 1 kN. A step-and-shoot procedure  
246 is followed to obtain  $\mu$ CT datasets of the fabric layer and the spacing between the  
247 compression platens. At different pressure levels, each  $\mu$ CT scan is made in  
248 approximately 10 minutes using the Environmental Micro-CT system (EMCT) at Ghent  
249 University [29]. During this time, the position of the compression platens remains  
250 stationary, and a slight relaxation of the pressure by 1.5% of the set pressure value was  
251 observed for the two highest pressure levels. No movement artefacts were observed in the  
252  $\mu$ CT scan, indicating that the relaxation in the sample and PEEK compression platens  
253 during scanning were smaller than the image resolution, and thus did not affect imaging.  
254 For each scan, a total of 1440 projection images are acquired during a rotation of the  
255 scanner setup around the object from  $0^\circ$  to  $360^\circ$ . The X-ray source is operated with a  
256 source accelerating voltage of 80 kV, with a power of 8 W. Tomographic reconstruction  
257 is performed using Octopus Reconstruction [30]. The load is recorded by the CT5000  
258 testing stage and combined with the displacement data measured on the  $\mu$ CT images.

259 The fabric under consideration has a thickness of approximately 0.5 mm in a non-  
260 compressed state and is compressed to approximately 0.25 mm. Hence, to have an  
261 adequate pressure-thickness or pressure-volume fraction curve, the distance between the  
262 compression platens needs to be accurately monitored at the micrometer scale. Studies  
263 often analyze the compressive properties by compression of multiple layers of  
264 reinforcement, e.g. [31–33]. This is advantageous for the platen-to-platen measurement  
265 accuracy since it results in a larger spacing between the compression platens, which in  
266 turn allows for the use of less sensitive displacement measurements such as the crosshead  
267 displacement. Nevertheless, the resulting compression curve is not representative for a  
268 single ply of reinforcement due to nesting of the layers and thus cannot be used to validate  
269 the model here.



270

271  
272

**Figure 3** – (a) Setup 1: self-aligning compression setup, (b) Setup 2: in-situ compression setup for  $\mu$ CT measurements.

273 In addition to the compressive experiments, four composite specimens were produced by  
 274 compression moulding of a single fabric reinforcement layer between two flat plates  
 275 under a pressure of 0.0, 0.5, 0.12 and 0.25 MPa applied by stacking weights on top of the  
 276 plate. These specimens were then cured at room temperature (matrix resin is EPIKOTE  
 277 MSG RIMR 135 and EPIKURE MGS RIMH 137 from Momentive Performance  
 278 Materials, Hemiksem, Belgium) and subsequently  $\mu$ CT images were obtained to  
 279 determine the thickness of the specimens.

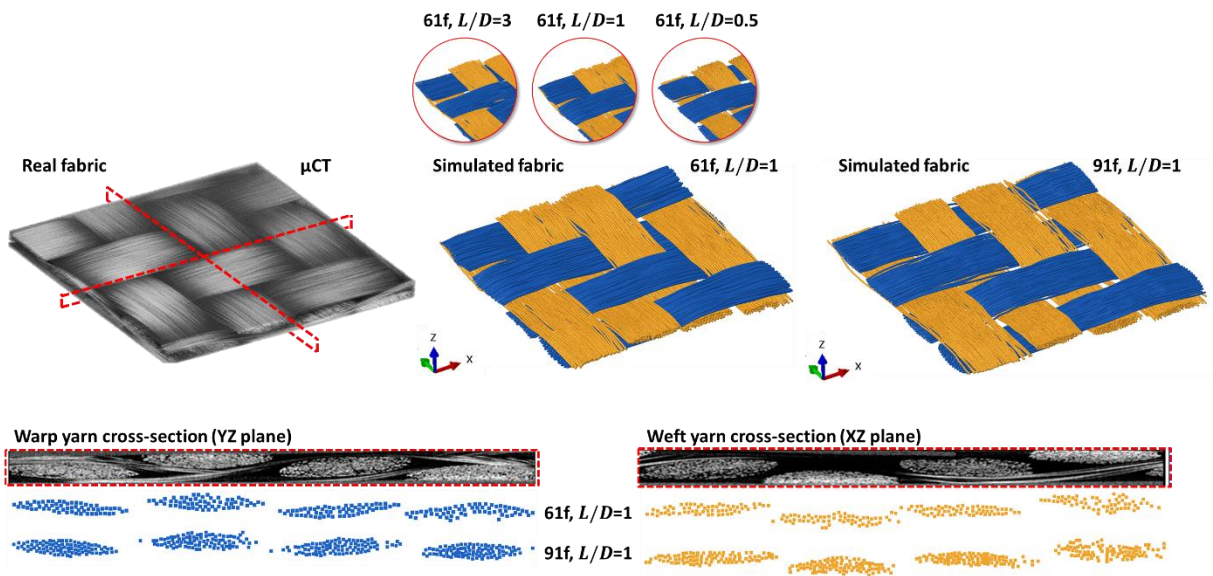
## 280 4. Results and Discussion

### 281 4.1. Generation of the as-woven state through virtual fiber modeling

282 **Figure 4** represents the as-woven states for yarns made up of 61 and 91 virtual fibers.  
 283 These numbers were based on earlier work. For example, Green *et al.* [15] studied the  
 284 effect of the number of virtual fibers per yarn, going from 19 to 91, and indicated that at  
 285 least two or three virtual fibers across the thickness of the yarns in their deformed state  
 286 where required for sufficient accuracy. In their case, a 61 fiber model represented the best  
 287 compromise between analysis time and accuracy, and only very minor improvements  
 288 were noted using 91 fibers. Similarly, the results in Figure 4 indicate that 61 virtual fibers  
 289 suffice here as well.

290 The predicted fabric geometry (fabric thickness, yarn widths, cross-sectional shapes)  
 291 corresponds well to that of the actual fabric. The as-woven state is simulated using the  
 292 Abaqus/Explicit solver with dynamics similar to the actual weaving process: a step time  
 293 of 0.06 s corresponding to a weaving speed of 1000 picks/min, a typical value for

294 projectile, rapier and air-jet looms. Three different length-to-diameter ratios for the truss  
 295 elements and beam overlay elements were investigated, i.e.  $L/D$  equals 0.5, 1, or 3 (see  
 296 Section 4.3.1). The *General Contact* algorithm in Abaqus 2019 performed well for each  
 297  $L/D$  ratio considered here and contact/collision detection remained robust even for much  
 298 larger  $L/D$  ratios. Nevertheless, large  $L/D$  ratios are not feasible as they would affect the  
 299 “flexibility” of a virtual fiber (in the digital element method, material properties are  
 300 induced by discretization into elements, in contrast to finite element modeling where they  
 301 are defined by the material constitutive laws).



302

303 **Figure 4** – Comparison of real fabric from  $\mu$ CT experiments (left) and simulated fabric (micro-)geometry (right)  
 304 shows good visual agreement between both.

305

306 **4.2. Experimental determination of the through-thickness compressive response**  
 307 **of a single fabric layer**

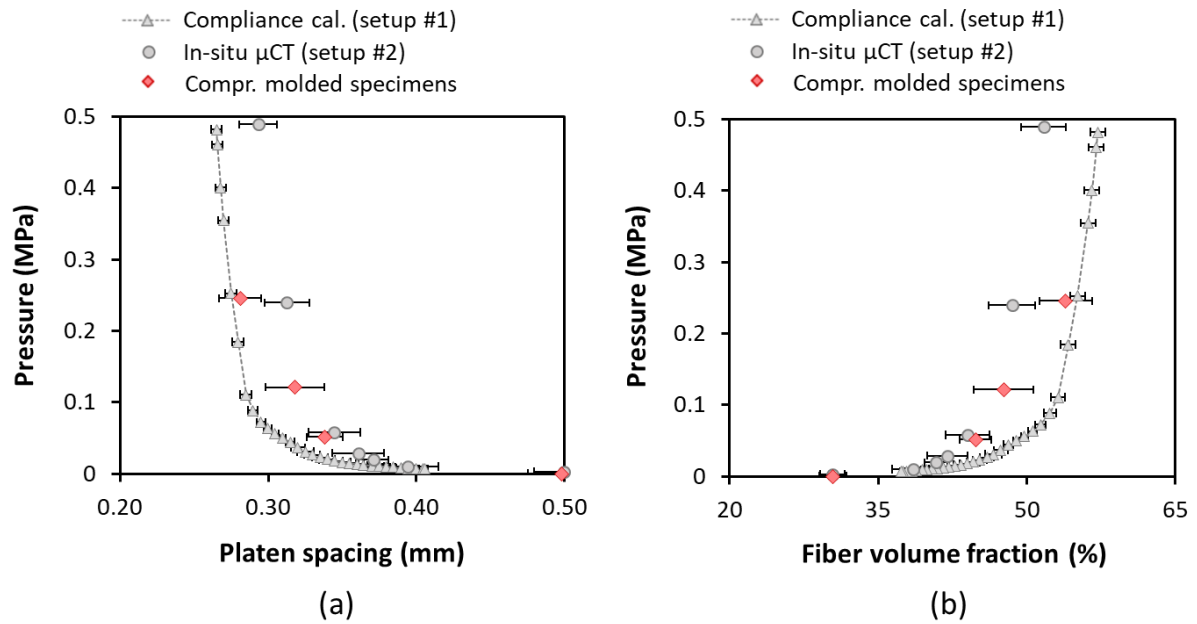
308 The compressive response of the fabric measured according to the different  
 309 methods/setups explained in Section 3.2 is given in **Figure 5** (fiber volume fraction was  
 310 determined based on the fiber density, fabric areal density and platen-to-platen distance).  
 311 Overall, the curves show an exponentially increasing pressure for higher compression  
 312 levels as expected. As a comparison, the thickness of the molded composite specimens  
 313 are added as well (red datapoints).

314 The compliance calibration procedure using crosshead displacement data seems to result  
 315 in an underestimation of the platen-to-platen distance (fabric thickness), especially in the  
 316 low compression regime (here 0.0 – 0.2 MPa). This could have several causes, e.g. (i) the

317 platen-to-platen misalignment is not identical during recording of the calibration curve  
318 and the specimen curves, or, (ii) the set-up compliance is not perfectly reproducible due  
319 to spurious misalignments in the fixtures or testing machine. Since there is no physical  
320 measurement of the actual platen-to-platen distance, it remains difficult to assess whether  
321 the response in the low compression regime can be considered correct.

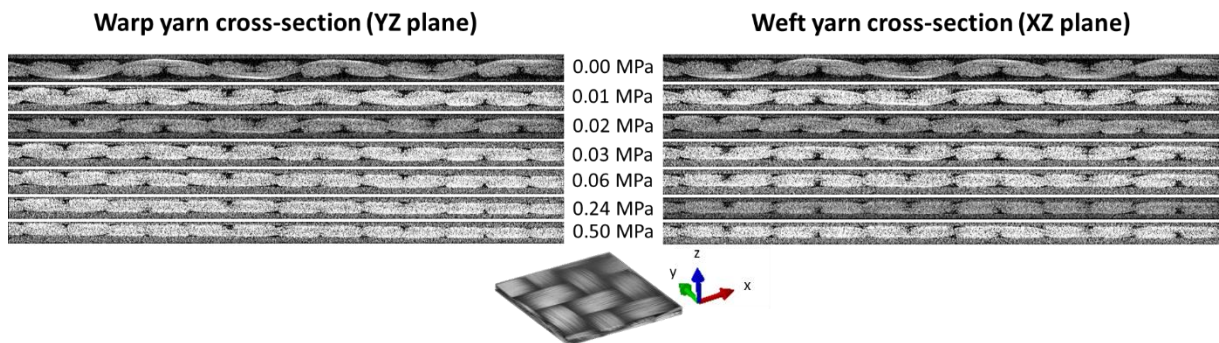
322 Using in-situ  $\mu$ CT during compressive testing did allow to determine the physical platen-  
323 to-platen distance at each pressure level from the  $\mu$ CT images (**Figure 6**). There is good  
324 agreement with the results from the compression molded specimens, especially in the low  
325 pressure regime. At the specimen size required for sufficient unit cells to be loaded under  
326 compression, however, the resolution of the  $\mu$ CT-scans is approximately 15  $\mu$ m.  
327 Moreover, the use of the in-situ compression test set-up and the limited platen-to-platen  
328 distance (platens made from PEEK polymer) inevitably lowered the quality of the  $\mu$ CT  
329 images. This means that there is an uncertainty of 1 – 2 voxels on the determination of  
330 the borders of the compression platens, which results in the relatively large error bars  
331 compared to the compliance calibration method in Figure 5. In comparison to the  
332 compliance calibration method, the compression set-up used in the  $\mu$ CT scanner is not  
333 self-aligning and maintains a fixed platen misalignment of approximately  $0.25^\circ$  in both  
334 warp and weft direction (determined on the  $\mu$ CT images).

335 Overall, the experimental compressive response of one reinforcement ply remains  
336 difficult to assess with adequate certainty. Therefore, the range described by both the  
337 compliance calibration and the in-situ  $\mu$ CT method is considered as the validation  
338 window for the simulations.



339

340 **Figure 5** – (a) Pressure versus platen spacing and (b) pressure versus fiber volume fraction obtained by the three  
 341 different setups. These results clearly illustrate the difficulty associated with measuring the through-thickness  
 342 compressive response of a single fabric layer with adequate certainty.



343

344

**Figure 6** –  $\mu$ CT images of the yarn cross-sections during compression.

345

### 346 **4.3. Simulating the through-thickness compressive response**

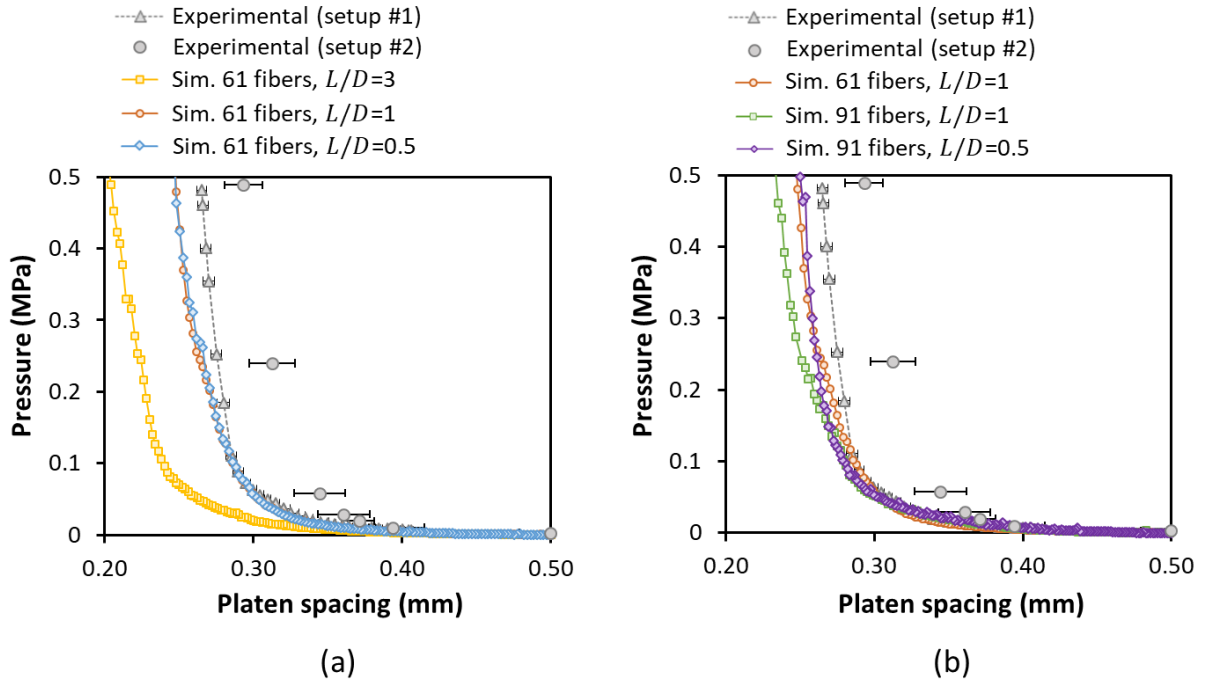
#### 347 **4.3.1. Mesh convergence**

348 Although the simulation of the as-woven state is not affected much by the considered  
 349  $L/D$ -ratios, this is different for the compression simulations using the beam element  
 350 overlay (**Figure 7a**). During compression, virtual fibres are bent around other off-axis  
 351 virtual fibers. Hence, the element length needs to be similar to the virtual fiber diameter  
 352 to conform to the geometry of the neighbouring off-axis fibers. The (bending) strain  
 353 energy of the superimposed beam elements was indeed higher for  $L/D$  ratios of 1 and 0.5  
 354 compared to a ratio of 3, indicating a higher degree of bending happening in the virtual

355 fibres for  $L/D$  ratios of 1 and 0.5. This explains why a stiffer compaction response is  
356 recorded for these simulations. Here an  $L/D$  ratio  $\leq 1$  sufficed to achieve convergence of  
357 the simulations using 61 virtual fibres, and  $L/D = 1$  is selected for further simulations  
358 (reduced computational resources compared to  $L/D = 0.5$ ).

359 Beside the element length, the number of virtual fibers can also be seen as a mesh  
360 convergence parameter (e.g. dividing the yarn into a very small amount of virtual fibers  
361 would not lead to the same results). The results (**Figure 7b**) show that the difference for  
362 61 and 91 fibers is small, taking into account that both simulations are run with the same  
363 frictional constant albeit that the yarns have a differing internal frictional surface (more  
364 detailed explanation in **Section 4.3.3**). Hence, we can assume that the compression  
365 simulations have also converged at 61 virtual fibers. This is in close agreement with the  
366 required number of virtual fibers reported by other research groups [34,35]. Note that a  
367 compression simulation for 61 virtual fibers with  $L/D = 1$  took about 6 hours of  
368 calculation time on a regular PC (Intel® Core™ i7-3770 3.40 GHz, 4 cores, 16.0 GB  
369 RAM, SSD hard disk). For the 91 virtual fibres, a difference in compression response is  
370 obtained above 0.2 MPa for  $L/D = 0.5$  and  $L/D = 1$ . Closer inspection of the results  
371 showed that for  $L/D = 1$  a higher amount of contact penetrations occurred at high  
372 compaction level than for  $L/D = 0.5$ , resulting in an (artificially) lower stiffness. This is  
373 explained in more detail in Section 4.3.5.





374

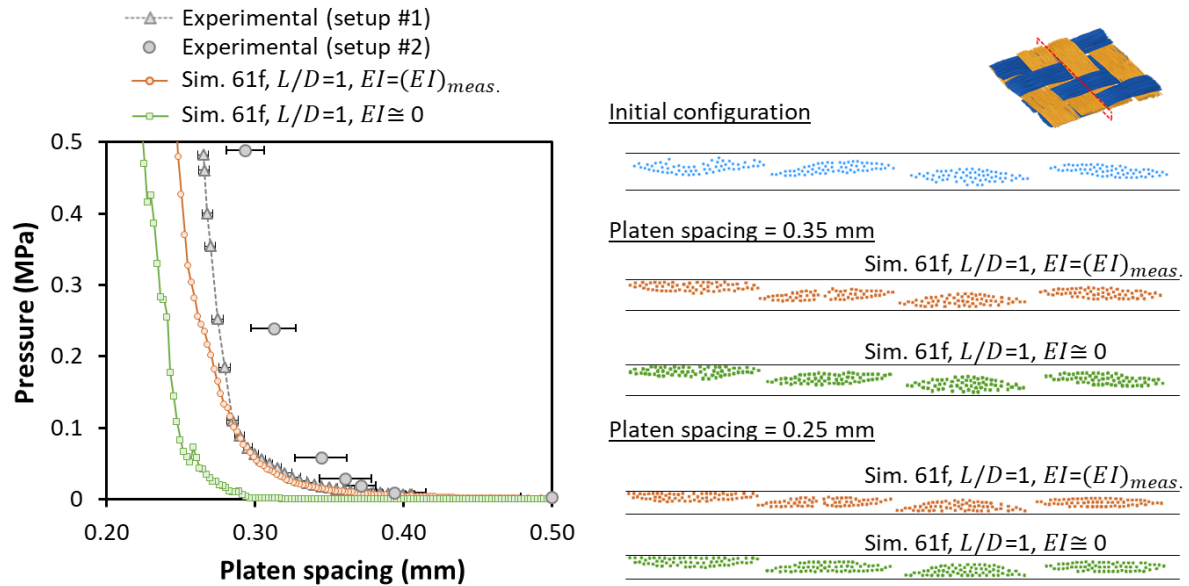
375 **Figure 7** – Compressive response for (a) different  $L/D$  ratios and (b) different amounts of virtual fibers per yarn  $n_{vf}$   
 376 show that the compressive response converges for  $L/D \leq 1$  and  $n_{vf} \geq 61$ .

377 The correspondence between the predicted and the experimentally determined  
 378 compaction response is good, especially at low compaction levels (up to 0.28 mm platen  
 379 spacing). This indicates that the compaction process is well captured by the virtual fibers,  
 380 even though there are size and number differences between the virtual and real fibers  
 381 which could lead to a difference in compaction (smaller fibers can compact more densely  
 382 than large fibers). In addition, simulations using parallel platens (misalignment of  $0^\circ$ ) or  
 383 using platens misaligned similarly to the experimental set-up (misalignment of  $0.25^\circ$  in  
 384 both x- and y-direction) resulted in almost identical results (not shown here). Therefor,  
 385 platen misalignment is not further considered in the simulations.

#### 386 4.3.2. Bending stiffness

387 The need to add virtual fiber bending stiffness to the simulation is illustrated in **Figure 8**  
 388 by the difference in the compression reaction force of the fabric when bending stiffness  
 389 is and is not present. Simulations performed without any bending stiffness mainly show  
 390 a kinematic response where initially the reaction force is predominantly determined by  
 391 the ease with which the (virtual) fibers can be rearranged in the structure by the  
 392 compression platens (densification). The reaction force on the platens only increases at  
 393 high compression levels when fiber realignment becomes obstructed and the fibers  
 394 become transversally loaded. On the other hand, when including fiber bending stiffness,

395 the kinematics remain fairly similar, but an additional compressive reaction force is noted,  
 396 especially in the low pressure range. At this stage, the platens deform the virtual fibers by  
 397 bending – as well as realigning – them. The compressive response shows better agreement  
 398 with the experimentally determined curve, both in terms of its shape and its position.



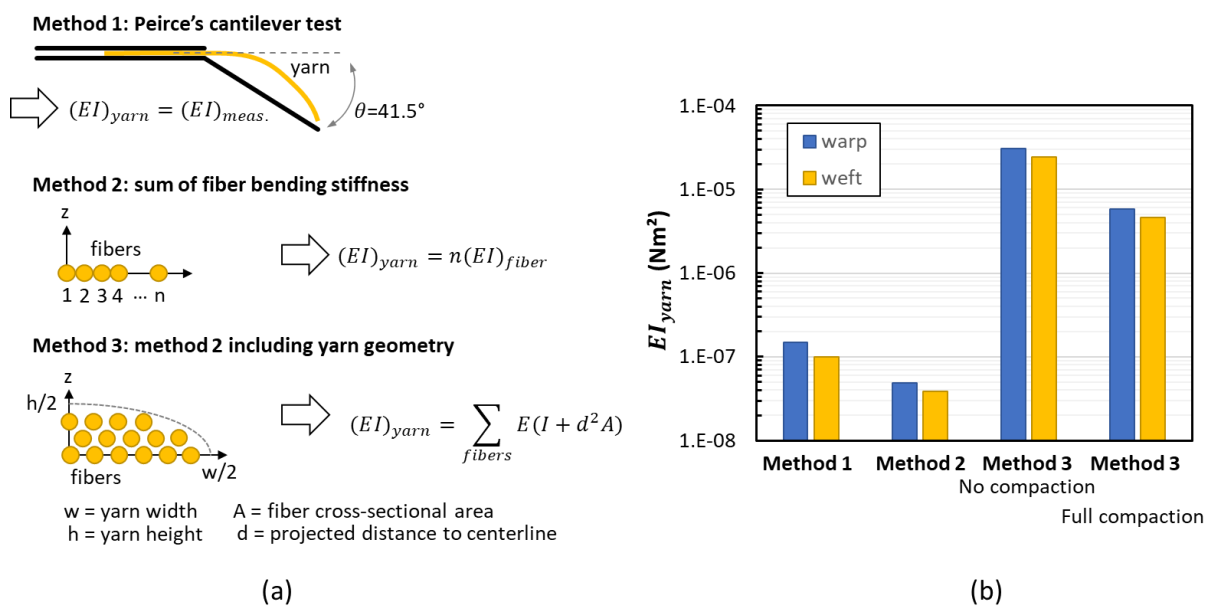
399

400 **Figure 8** – Compressive response of fabric simulated with and without bending stiffness of the virtual fibers show  
 401 that while kinematically similar (yarn cross-sections are visualized on the right-hand side), the mechanical response  
 402 (left-hand side) is better predicted when bending stiffness is considered.

403 The question arises which value for the bending stiffness should be included in the  
 404 simulations. Experimentally, the bending stiffness of yarns is usually determined through  
 405 Peirce’s cantilever method (**Figure 9a**, method 1). Herein, the length of yarn required to  
 406 have a deflection of  $41.5^\circ$  under the yarn’s weight is recorded, which is then converted to  
 407 a bending stiffness in  $Nm$ . Although historically important and still widely used, the  
 408 method is limited since the bending stiffness is assumed to be constant and measured at  
 409 relatively high curvature. As yarns are a fibrous material, their cross-section easily  
 410 changes by realignment of the fibers. It is well-known that the yarns can flatten out at  
 411 high curvatures [36] which likely affects the results.

412 Theoretically, one can make an estimated guess of the yarn bending stiffness by using  
 413 beam theory to determine the bending stiffness of a single fiber within that yarn and  
 414 multiplying that value with the number of fibers present in the yarn (Figure 9a, method 2).  
 415 This corresponds to the assumption that the yarn is made up of fibers all lying next to  
 416 each other on the yarn’s heart line without any interaction between them. Hence such a  
 417 value underestimates the actual yarn bending stiffness. If the position of each of the fibers

418 within the yarn envelope is known, a more realistic approximation of the yarn bending  
 419 stiffness could be made using the parallel axis theorem. The distance between the fiber  
 420 bending axis and the yarn bending axis then causes an additional increase in the calculated  
 421 yarn bending stiffness (Figure 9a, method 3). An idealized approximation of the fiber  
 422 positions can be made a priori by assuming that they all lie evenly spaced in layers with  
 423 a height equal to the fiber diameter in an ellipsoidal configuration that represents the  
 424 cross-section of the yarn. This assumption would only require the yarn width and height  
 425 and the number of fibers per yarn and should give a ballpark number for the yarn bending  
 426 stiffness (not considering fiber-to-fiber interaction).



427

428 **Figure 9** - (a) Calculation of the yarn bending stiffness  $(EI)_{yarn}$  through three different methods, and (b) the  
 429 resulting values of  $(EI)_{yarn}$ . These results show that the experimentally determined  $(EI)_{yarn}$  is at the lower  
 430 bound of the theoretically calculated range. This indicates that the bending stiffness of the yarns is predominantly  
 431 determined by the bending stiffness of the individual fibers and much less by their position within the yarn's cross-  
 432 section, which in turn indicates that fiber realignment is a major deformation mechanism during yarn bending.

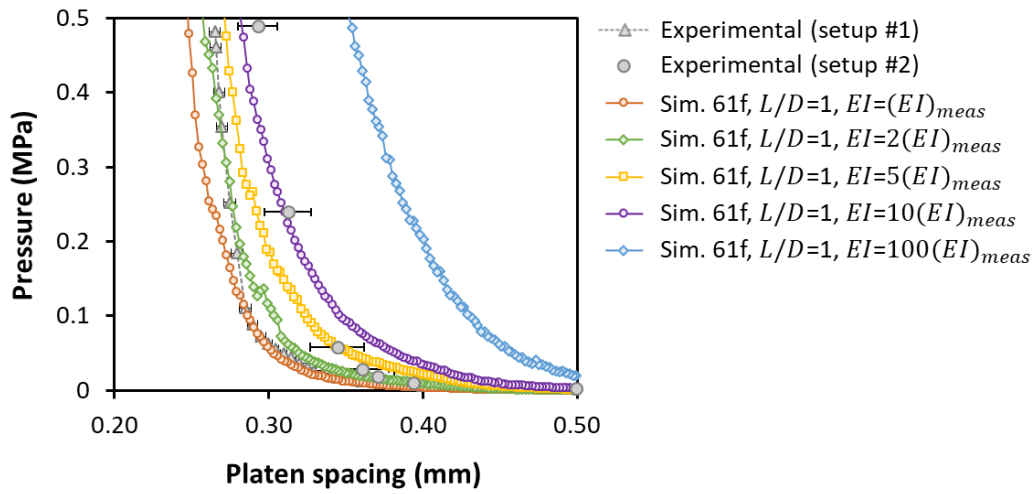
433 **Figure 9b** shows the values for the bending stiffness that are determined according to the  
 434 methods described in the previous two paragraphs (experimentally, theoretically without  
 435 the parallel axis theorem, and theoretically with the parallel axis theorem at two  
 436 compression levels). It is worth noting that the experimentally determined bending  
 437 stiffness  $(EI)_{measured}$  falls within the range determined by the idealized theoretical  
 438 calculations which span about three orders of magnitude. Furthermore,  $(EI)_{measured}$  is  
 439 closer to the predicted bending stiffness without applying the parallel axis theorem for  
 440 the initial yarn shape (height and width measured from  $\mu$ CT images). This is further  
 441 indication – at least at a curvature responsible for the yarn making a  $41.5^\circ$  angle in

442 Peirce’s cantilever experiment – that the measured bending stiffness is strongly  
443 influenced by “flattening” of the yarn. This shows that fiber realignment, and the  
444 accompanying cross-section change, is a dominant deformation mechanism during the  
445 bending of yarns.

446 Note that Equation 2, used to determine the value of the bending stiffness imposed on  
447 each individual virtual fiber, does not take into account the position of the virtual fibres  
448 within the yarn and thus does not use the parallel axis theorem. However, as the number  
449 of virtual fibers is rather small, the difference in  $EI$  determined according to ‘method 2’  
450 and ‘method 3’ is only around one order of magnitude for the virtual yarns, compared to  
451 three orders of magnitude for the real yarns.

452 Despite these complications, Equation 2 is applied and  $(EI)_{yarn} = (EI)_{measured}$  is used  
453 as a baseline in the simulations to induce a bending stiffness in the virtual fibers, as  
454 bending stiffness measurements according to Peirce’s method are readily available in  
455 literature. **Figure 10** shows the effect of increasing the bending stiffness by two orders of  
456 magnitude on the compressive response of the simulated fabric. Firstly, one can see that  
457 the simulations correlate well with the experimentally determined compressive behavior,  
458 especially when taking into account the uncertainty on the experimental bending stiffness  
459 measurements. For the baseline bending stiffness, the thickness of the fabric at a certain  
460 pressure is slightly underestimated. The overall shape of the simulated compressive curve  
461 is however close to the experimental compressive, which indicates that the simulation  
462 does take the correct deformation mechanisms (e.g. yarn flattening, fiber realignment, ...)   
463 into account. The agreement between simulation and experiment improves (slightly) for  
464 a bending stiffness 2 or 5 times the base bending stiffness. At even higher bending  
465 stiffness of 10 and 100 times  $(EI)_{measured}$ , the compressive response at low compression  
466 levels is overestimated, indicating that values in this range are too high. Hence, these  
467 simulations show that using Peirce’s cantilever method results in an adequate value for  
468 the yarn bending stiffness, perhaps slightly underestimating it. Nevertheless, it might be  
469 worthwhile to consider other test methods in the future that allow recording of the  
470 moment-curvature relationship to obtain better input parameters, e.g. by using apparatus  
471 similar to the Kawabata Evaluation System for Fabrics or the set-up described in Ref.  
472 [37]. Another possibility would be to explicitly model Peirce’s cantilever experiment  
473 using virtual fibers to inversely determine the correct  $(EI)_{yarn}$ , but the large

474 displacements required under quasi-static conditions make this approach unfeasible with  
 475 the current set-up.



476

477 **Figure 10** – Effect of the bending stiffness of the virtual fibers on the compressive response of the simulated fabric.  
 478 A better agreement between the simulated and experimental responses is obtained for a bending stiffness in the  
 479 range of 2 – 5 times the  $(EI)_{measured}$  (from Peirce’s cantilever method).

#### 480 4.3.3. Friction coefficient

481 Contrary to the as-woven simulation, there are (almost) no in-plane tensile forces active  
 482 during the through-thickness compression, and the deformation happens under quasi-  
 483 static conditions. Therefore, it is likely that the higher-bound friction coefficient of  
 484 0.3 – 0.4 is more appropriate. Note that there is only one frictional constant allowed in  
 485 the *General Contact* algorithm of the Abaqus 2019 solver, which determines the  
 486 interaction between all surfaces, i.e. fiber-to-fiber as well as fiber-to-platen.

487 Moreover, similar to the bending stiffness, the friction coefficient input value likely  
 488 depends on the discretization in digital fibers. Since the friction coefficient is typically  
 489 determined from yarn-to-yarn friction experiments, the amount of contacting surface area  
 490 is determined by the surface area of the fibers at the yarns’ outside perimeter. In addition,  
 491 as the fibers can realign themselves, intrayarn fiber-to-fiber friction also occurs, while  
 492 fibers that were present at the “inside” of the yarn might migrate towards the yarn  
 493 boundary depending on the deformation (e.g. at high compression level). Hence, the  
 494 yarn’s complete surface area  $A_{\mu,yarn}$ , determined by the cylindrical surface of each fiber,  
 495 comes into play during through-thickness compression. It is clear that this value is highly  
 496 dependent on the number of fibers as well as their diameter, according to the following  
 497 equation (per unit length):

$$A_{\mu,yarn} = n_{fiber}A_{\mu,fiber} = \pi n_{fiber}D_{fiber} \quad (3)$$

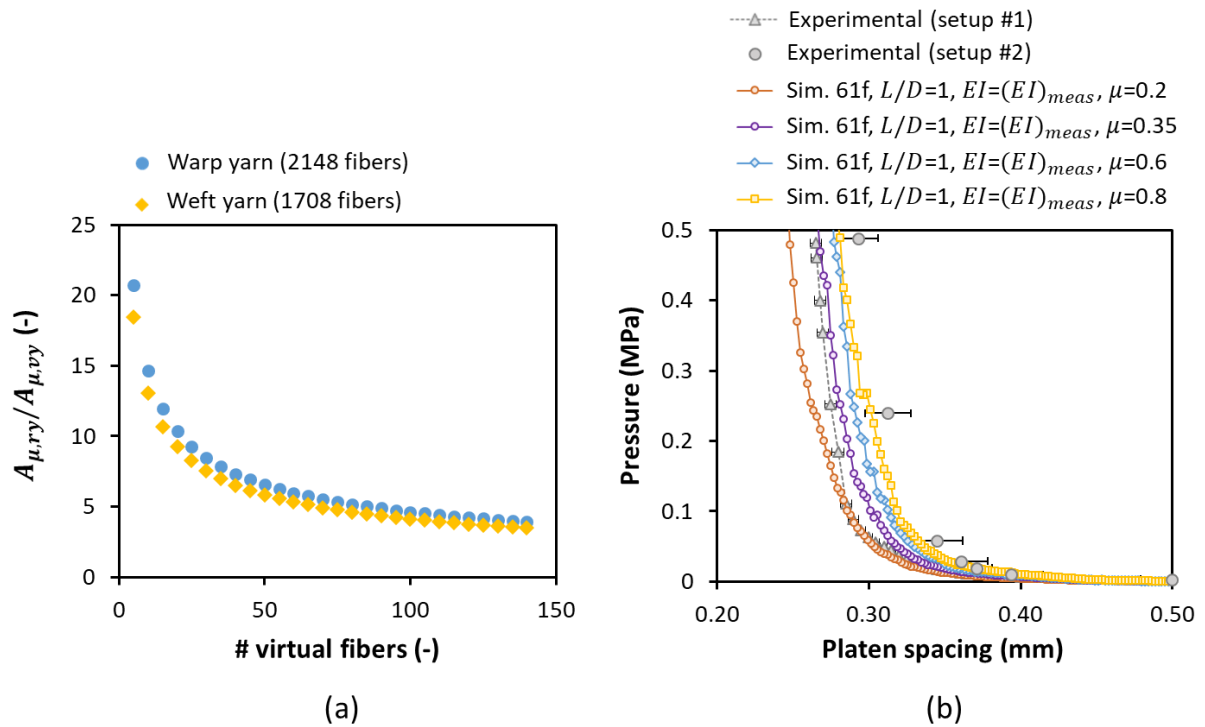
498

499 The ratio of the contact surface for the real yarn  $A_{\mu,ry}$  to that of the virtual yarn  $A_{\mu,vy}$  is  
 500 determined as:

$$\frac{A_{\mu,ry}}{A_{\mu,vy}} = \frac{n_{rf}D_{rf}}{n_{vf}D_{vf}} = \frac{n_{rf}}{n_{vf}} \left( \frac{n_{rf}}{n_{vf}} \right)^{-\frac{1}{2}} = \left( \frac{n_{rf}}{n_{vf}} \right)^{\frac{1}{2}} \quad (4)$$

501 and is found to be dependent only on the ratio of real to virtual fibers per yarn. For the  
 502 number of virtual fibers used here, i.e. 61 and 91, we thus estimate that the internal surface  
 503 area inside the real yarn is about 5 times higher than that inside the virtual yarn. This  
 504 shows that using the experimentally determined frictional coefficient as an input value in  
 505 the simulation likely results in an underestimation of the contact forces. However, one  
 506 cannot simply multiply this coefficient with a factor of 5, as the kinematics of the actual  
 507 fibers will also be different from those of the virtual fibers. For example, while the great  
 508 amount of small fibers in the real yarn results in a lot of potential contact surface, they  
 509 will also have more freedom to realign themselves and fill in empty gaps between other  
 510 fibers resulting in overall lower contact forces.

511 **Figure 11** shows the compressive response for simulations with  $EI_{yarn} = EI_{measured}$  for  
 512 a range of frictional constants from 0.2 – 0.4 which are still physically relevant and  
 513 correspond to the measured frictional constants, up to values of 0.8 which correspond to  
 514 artificially increased frictional constants. This shows that higher frictional constants  
 515 indeed lead to a better correlation between the simulation and the experiment as could be  
 516 expected. Nevertheless, in general, even a value of 0.35, which corresponds to the  
 517 measured value at low yarn pressure and low sliding speed, still produces acceptable  
 518 results (falls within the experimentally determined range) and is thus a good input  
 519 parameter.



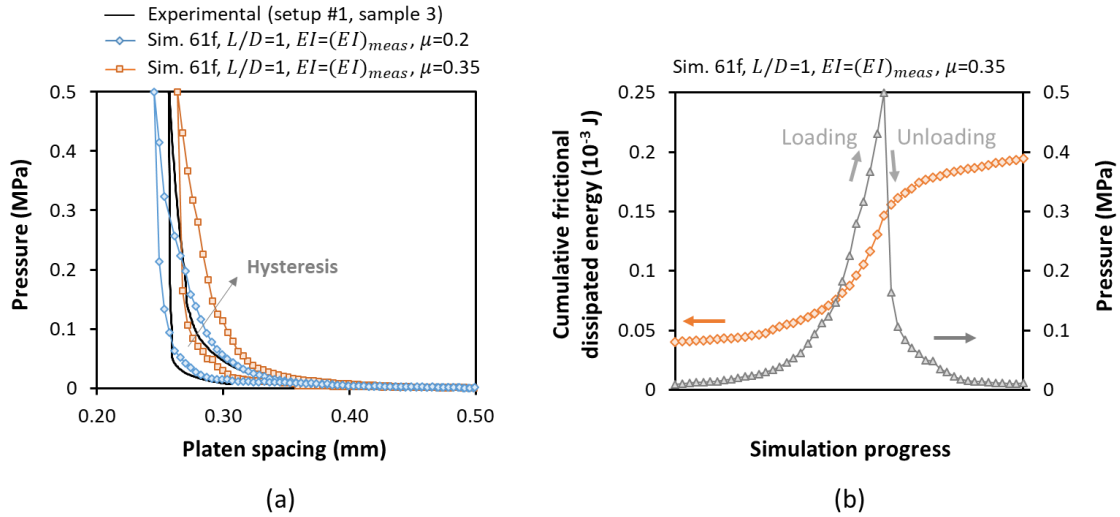
520

521 **Figure 11** – (a) Ratio of contact surface for the real yarn  $A_{\mu,ry}$  to that of the virtual yarn  $A_{\mu,vy}$  shows that at 61 – 91  
 522 virtual fibers per yarn, the virtual contact surface is about one fifth the size of the real contact surface. (b) The effect  
 523 of the frictional constant on the compressive response shows that higher frictional constants result in better  
 524 agreement with the experimentally determined response.

#### 525 4.3.4. Hysteresis – losses upon compression-unloading

526 The implementation of both bending stiffness, as well as friction into the virtual fiber  
 527 simulations, means that they can be predictive for (frictional) losses upon both  
 528 compressive loading and unloading. This is illustrated in **Figure 12a** and **Table 2** by a  
 529 range of simulations with different parameters (the losses are determined by the area  
 530 between the loading-unloading curve). The experimental losses were determined from  
 531 the loading-unloading curves obtained through the compliance-calibration procedure  
 532 (setup #1). In both simulation and experiment, the fabric is loaded monotonically to  
 533 0.5 MPa and immediately unloaded at the same speed while the load-displacement curve  
 534 is recorded. The results in Table 2 show that the hybrid virtual fibers are indeed capable  
 535 of simulating hysteresis losses during compression-unloading of a single fabric and the  
 536 agreement between the experimental and simulated values is good. Moreover, the  
 537 hysteresis losses seem relatively independent from input parameters such as the bending  
 538 stiffness and the frictional constant. **Figure 12b** shows the (cumulative) frictional  
 539 dissipated energy (obtained from the history output data in Abaqus) in function of the  
 540 simulation progress (time). In each of the hysteresis simulations, the trend in frictional

541 dissipated energy was similar, with the strongest increase in dissipated energy happening  
 542 at the end of the loading step (compaction). Furthermore, after the sharp drop in pressure  
 543 during unloading, the frictional dissipated energy keeps increasing, albeit at a lower rate.  
 544 This indicates fiber movement which corresponds to a recovery of the (bending) stresses  
 545 and spring back of the fibers.



546

547 **Figure 12** – (a) Experimental and simulated (61 fibers,  $L/D=1$ ,  $EI=(EI)_{meas}$ ,  $\mu=0.2$ , and 61 fibers,  $L/D=1$ ,  
 548  $EI=(EI)_{meas}$ ,  $\mu=0.35$ ) loading-unloading compressive response of a single fabric layer. Overall, the curve shape is  
 549 well predicted by the simulations with an immediate and large drop in pressure at the start of unloading. (b) The  
 550 frictional dissipated energy obtained from the history output data of Abaqus in function of simulation progress  
 551 shows that the main frictional dissipation occurred at high compaction pressures during the loading step . After the  
 552 immediate pressure drop during unloading, the frictional dissipated energy still increases slightly, indicating some  
 553 fiber movement during unloading (spring back).

554

555 **Table 2** – Hysteresis losses during loading-unloading of the fabric layer. The experimental value is determined from  
 556 the curves obtained by the compliance-calibration procedure (setup #1). The simulated values are higher, but  
 557 correspond well to the experimental value.

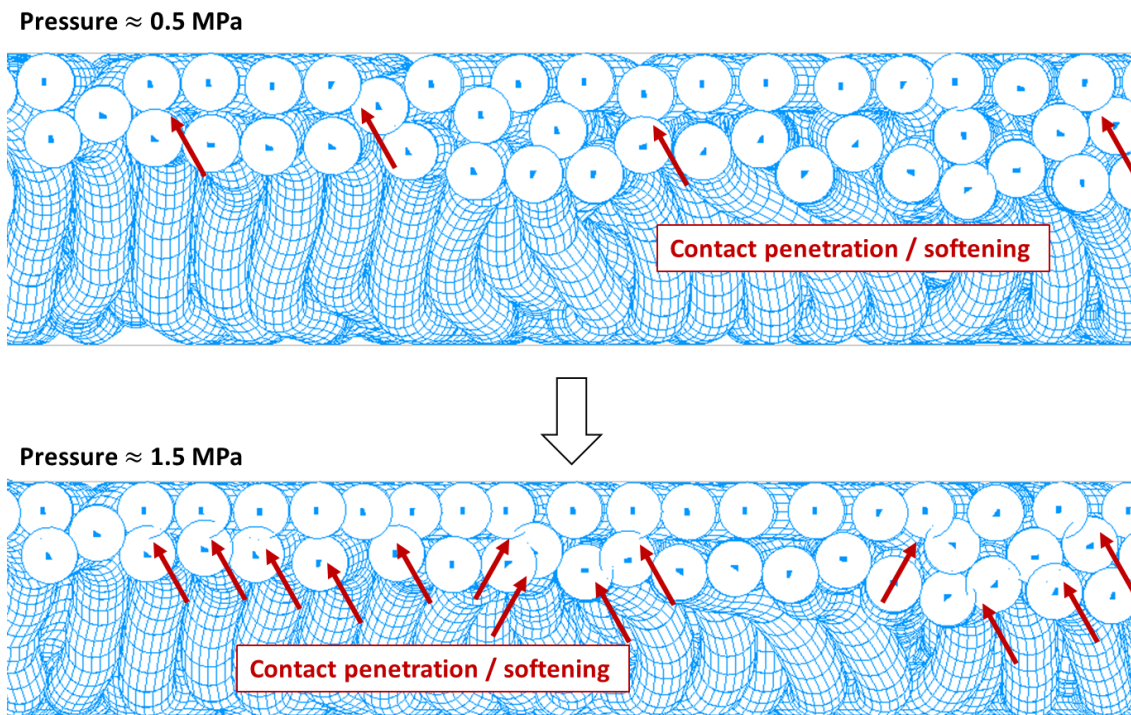
Experiment					Hysteresis losses (J/m <sup>2</sup> )
					6.72 ± 0.24
Simulation	# virtual fibers	L/D	EI	μ	
	61	1	$EI_{meas}$	0.2	7.62
	61	1	$EI_{meas}$	0.35	8.04
	61	1	$EI_{meas}$	0.6	7.15
	61	1	$EI_{meas}$	0.8	7.06
	61	1	$2EI_{meas}$	0.35	7.92

558



4.3.5. Contact problems arising at high pressure levels

559 The *General Contact* algorithm implemented in Abaqus/Explicit is very robust at  
560 detecting colliding/contacting surfaces for truss elements. Yet it is a kinematically  
561 enforced algorithm, meaning that in each time step, the surfaces are allowed to move  
562 “into” each other at a ratio of  $k$  (penalty stiffness), resulting in an opposing contact force  
563 which is then iterated and resolved to have proper surface-to-surface contact. The  
564 downside to such an algorithm – in this case – is that numerical softening (and damping)  
565 is required. The softening prevents extreme static loadings. This might be a reason why  
566 the simulated compressive response is always slightly lacking in stiffness at high  
567 compression (lower slope compared to the experimental data, see e.g. Figure 10). More  
568 importantly, with the current implementation using the standard numerical settings, where  
569 the penalty stiffness is automatically determined by the software based on the material  
570 properties, the amount of compressive pressure is limited to approximately 1 MPa. At  
571 pressures above this value, the penetration of contacting surfaces becomes very prominent  
572 and affects the predictive capability of the simulation method as the fabric thickness is  
573 underestimated, see **Figure 13**. Nevertheless, pressures relevant for vacuum infusion and  
574 autoclave production from 0 – 8 bar remain viable.  
575



576

577 **Figure 13** – Contact overclosures/penetrations (softening) between neighboring fibers occur in large amounts at  
578 pressures above 1 MPa.

579 **5. Conclusions**

580 The results clearly show the potential for the virtual fiber modeling method including  
581 fiber bending stiffness as a general textile modeling framework. Taking our previous  
582 work on in-plane properties into account [18,19], the addition of out-of-plane property  
583 simulation capabilities indicates that a large range of textile-relevant loadings can be  
584 considered. This approach, fully implemented in the commercial finite element software  
585 package Abaqus using the standard element, material and contact libraries, allows  
586 research groups with FEA experience but without dedicated virtual fiber tools to  
587 implement this type of modeling. Good agreement is obtained between the experimental  
588 and the numerical determined pressure-compression behavior. The macroscopic  
589 compressive response of the fabric is well predicted for the right set of input parameters.  
590 Moreover, the microscale deformation mechanisms are captured as well, resulting in good  
591 agreement with  $\mu$ CT-scans and prediction of hysteresis-losses due to fiber realignment  
592 and friction.

593 On the other hand, the results also show that improvements are still required. For example,  
594 an  $L/D$  element ratio of 1 was used in this work, but larger ratios could improve  
595 computation time. Yet, here,  $L/D$  ratios of 3 result in non-converged solutions. One  
596 possible solution could be the use of non-constant element lengths along the fiber to  
597 reduce the number of elements while maintaining convergence. On the input property  
598 side, the friction coefficient and bending stiffness that should be implemented remain  
599 difficult to assess. Although the results have shown that the simulation output is rather  
600 robust for a wide range of input properties, it would be best to determine which values  
601 are most appropriate. Future studies could, for example, consider a numerical calibration  
602 of the material parameters by using a 1-to-1 simulation-experimental approach, where the  
603 -previously experimental - friction and bending stiffness experiments are explicitly  
604 modeled using virtual fibers. In addition, more complex material behavior such as non-  
605 linear bending and non-linear friction can be included to increase the prediction accuracy.  
606 To extend the method to high-pressure LCM processes, a robust contact algorithm with  
607 minimal contact penetration is required.

608 Overall, the proposed methods allow a predictive analysis of fabric compression behavior  
609 and are thus well-suited to analyze and optimize fabric structures for example in LCM  
610 manufacturing processes.

611 **6. Acknowledgments**

612 Financial support from Research Foundation – Flanders (FWO) is gratefully  
613 acknowledged. Results in this paper were obtained within the framework of the FWO  
614 grant 12ZR520N. For the CT5000 load cell, FCWO – Ugent, as well as FWO is  
615 acknowledged under the project G.0041.15N. The Centre of Expertise UGCT is  
616 supported by the Ghent University Special Research Fund (BOF.EXP.2017.0007). We  
617 acknowledge the Swiss Competence Center for Energy Research (SCCER) Mobility of  
618 the Swiss Innovation Agency (Innosuisse) and the Swiss National Science Foundation  
619 (SNF - 182669) for financial support.

## 620 7. Bibliography

- 621 [1] J. Hemmer, C. Burtin, S. Comas-Cardona, C. Binetruy, T. Savart, A. Babeau, Unloading during  
622 the infusion process: Direct measurement of the dual-scale fibrous microstructure evolution with  
623 X-ray computed tomography, *Compos. Part A Appl. Sci. Manuf.* 115 (2018) 147–156.  
624 doi:10.1016/j.compositesa.2018.09.013.
- 625 [2] W. Huang, P. Causse, H. Hu, S. Belouettar, F. Trochu, Transverse compaction of 2D glass woven  
626 fabrics based on material twins – Part I: Geometric analysis, *Compos. Struct.* 237 (2020) 111929.  
627 doi:10.1016/j.compstruct.2020.111929.
- 628 [3] M.A. Ali, R. Umer, K.A. Khan, W.J. Cantwell, In-plane virtual permeability characterization of  
629 3D woven fabrics using a hybrid experimental and numerical approach, *Compos. Sci. Technol.*  
630 173 (2019) 99–109. doi:10.1016/j.compscitech.2019.01.030.
- 631 [4] Y. Mahadik, K.A.R. Brown, S.R. Hallett, Characterisation of 3D woven composite internal  
632 architecture and effect of compaction, *Compos. Part A Appl. Sci. Manuf.* 41 (2010) 872–880.  
633 doi:10.1016/j.compositesa.2010.02.019.
- 634 [5] T. Centea, P. Hubert, Measuring the impregnation of an out-of-autoclave prepreg by micro-CT,  
635 *Compos. Sci. Technol.* 71 (2011) 593–599. doi:10.1016/j.compscitech.2010.12.009.
- 636 [6] S.C. Garcea, Y. Wang, P.J. Withers, X-ray computed tomography of polymer composites,  
637 *Compos. Sci. Technol.* 156 (2018) 305–319. doi:10.1016/j.compscitech.2017.10.023.
- 638 [7] S. Yan, X. Zeng, L. Brown, A. Long, Geometric modeling of 3D woven preforms in composite  
639 T-joints, *Text. Res. J.* 88 (2018) 1862–1875. doi:10.1177/0040517517712098.
- 640 [8] Z. Yousaf, P. Potluri, F. Léonard, P. Withers, Meso scale analysis of 2D glass woven preforms  
641 under compaction, in: *ICCM Int. Conf. Compos. Mater., International Committee on Composite  
642 Materials*, 2013: pp. 392–399.
- 643 [9] M. Valkova, D.B. Anthony, A.R.J. Kucernak, M.S.P. Shaffer, E.S. Greenhalgh, Predicting the  
644 compaction of hybrid multilayer woven composite reinforcement stacks, *Compos. Part A Appl.  
645 Sci. Manuf.* 133 (2020) 105851. doi:10.1016/j.compositesa.2020.105851.
- 646 [10] Y. Wang, X. Sun, Digital-element simulation of textile processes, *Compos. Sci. Technol.* 61  
647 (2001) 311–319. doi:10.1016/S0266-3538(00)00223-2.
- 648 [11] G. Zhou, X. Sun, Y. Wang, Multi-chain digital element analysis in textile mechanics, *Compos.  
649 Sci. Technol.* 64 (2004) 239–244. doi:10.1016/S0266-3538(03)00258-6.
- 650 [12] O. Döbrich, T. Gereke, C. Cherif, Modeling the mechanical properties of textile-reinforced  
651 composites with a near micro-scale approach, *Compos. Struct.* 135 (2016) 1–7.  
652 doi:10.1016/j.compstruct.2015.09.010.
- 653 [13] D. Durville, I. Baydoun, H. Moustacas, G. Périé, Y. Wielhorski, Determining the initial  
654 configuration and characterizing the mechanical properties of 3D angle-interlock fabrics using  
655 finite element simulation, *Int. J. Solids Struct.* (2017). doi:10.1016/j.ijsolstr.2017.06.026.
- 656 [14] D. Durville, Simulation of the mechanical behaviour of woven fabrics at the scale of fibers, *Int. J.  
657 Mater. Form.* 3 (2010) 1241–1251. doi:10.1007/s12289-009-0674-7.
- 658 [15] S.D. Green, A.C. Long, B.S.F. El Said, S.R. Hallett, Numerical modelling of 3D woven preform  
659 deformations, *Compos. Struct.* 108 (2014) 747–756. doi:10.1016/j.compstruct.2013.10.015.
- 660 [16] Y. Mahadik, S.R. Hallett, Finite element modelling of tow geometry in 3D woven fabrics,  
661 *Compos. Part A Appl. Sci. Manuf.* 41 (2010) 1192–1200.  
662 doi:10.1016/j.compositesa.2010.05.001.
- 663 [17] L. Huang, Y. Wang, Y. Miao, D. Swenson, Y. Ma, C.-F. Yen, Dynamic relaxation approach with  
664 periodic boundary conditions in determining the 3-D woven textile micro-geometry, *Compos.*

- 665 Struct. 106 (2013) 417–425. doi:10.1016/j.compstruct.2013.05.057.
- 666 [18] L. Daelemans, J. Faes, S. Allaoui, G. Hivet, M. Dierick, L. Van Hoorebeke, W. Van Paepegem,  
667 Finite element simulation of the woven geometry and mechanical behaviour of a 3D woven dry  
668 fabric under tensile and shear loading using the digital element method, *Compos. Sci. Technol.*  
669 137 (2016) 177–187. doi:10.1016/j.compscitech.2016.11.003.
- 670 [19] T.D.D. Dinh, A. Rezaei, L. Daelemans, M. Mollaert, D. Van Hemelrijck, W. Van Paepegem, A  
671 hybrid micro-meso-scale unit cell model for homogenization of the nonlinear orthotropic material  
672 behavior of coated fabrics used in tensioned membrane structures, *Compos. Struct.* 162 (2017)  
673 271–279. doi:10.1016/j.compstruct.2016.12.027.
- 674 [20] Z. Yousaf, P. Potluri, P.J. Withers, D. Mollenhauer, E. Zhou, S. Duning, Digital element  
675 simulation of aligned tows during compaction validated by computed tomography (CT), *Int. J.*  
676 *Solids Struct.* 154 (2018) 78–87. doi:10.1016/j.ijsolstr.2017.05.044.
- 677 [21] A.J. Thompson, B. El Said, D. Ivanov, J.P.H.P.-H. Belnoue, S.R. Hallett, High fidelity modelling  
678 of the compression behaviour of 2D woven fabrics, Elsevier Ltd, n.d.  
679 doi:10.1016/j.ijsolstr.2017.06.027.
- 680 [22] Q.T. Nguyen, E. Vidal-Sallé, P. Boisse, C.H. Park, A. Saouab, J. Bréard, G. Hivet, Mesoscopic  
681 scale analyses of textile composite reinforcement compaction, *Compos. Part B Eng.* 44 (2013)  
682 231–241. doi:10.1016/j.compositesb.2012.05.028.
- 683 [23] A. Charmetant, E. Vidal-Sallé, P. Boisse, Hyperelastic modelling for mesoscopic analyses of  
684 composite reinforcements, *Compos. Sci. Technol.* 71 (2011) 1623–1631.  
685 doi:10.1016/j.compscitech.2011.07.004.
- 686 [24] W. Wijaya, S. Bickerton, P.A. Kelly, Meso-scale compaction simulation of multi-layer 2D textile  
687 reinforcements: A Kirchhoff-based large-strain non-linear elastic constitutive tow model,  
688 *Compos. Part A Appl. Sci. Manuf.* 137 (2020) 106017. doi:10.1016/j.compositesa.2020.106017.
- 689 [25] A.J. Thompson, J.R. McFarlane, J.P.H. Belnoue, S.R. Hallett, Numerical modelling of  
690 compaction induced defects in thick 2D textile composites, *Mater. Des.* 196 (2020) 109088.  
691 doi:10.1016/j.matdes.2020.109088.
- 692 [26] L. Montero, S. Allaoui, G. Hivet, Characterisation of the mesoscopic and macroscopic friction  
693 behaviours of glass plain weave reinforcement, *Compos. Part A Appl. Sci. Manuf.* 95 (2017)  
694 257–266. doi:10.1016/j.compositesa.2017.01.022.
- 695 [27] D. Salvatori, B. Caglar, V. Michaud, 3D spacers enhance flow kinetics in resin transfer molding  
696 with woven fabrics, *Compos. Part A Appl. Sci. Manuf.* 119 (2019) 206–216.  
697 doi:10.1016/j.compositesa.2019.01.023.
- 698 [28] S. V. Lomov, L. Gorbatikh, Ž. Kotanjac, V. Koissin, M. Houille, O. Rochez, M. Karahan, L.  
699 Mezzo, I. Verpoest, Compressibility of carbon woven fabrics with carbon nanotubes/nanofibres  
700 grown on the fibres, *Compos. Sci. Technol.* 71 (2011) 315–325.  
701 doi:10.1016/j.compscitech.2010.11.024.
- 702 [29] M. Dierick, D. Van Loo, B. Masschaele, J. Van Den Bulcke, J. Van Acker, V. Cnudde, L. Van  
703 Hoorebeke, Recent micro-CT scanner developments at UGCT, *Nucl. Instruments Methods Phys.*  
704 *Res. Sect. B Beam Interact. with Mater. Atoms.* 324 (2014) 35–40.  
705 doi:10.1016/j.nimb.2013.10.051.
- 706 [30] J. Vlassenbroeck, M. Dierick, B. Masschaele, V. Cnudde, L. Van Hoorebeke, P. Jacobs, Software  
707 tools for quantification of X-ray microtomography at the UGCT, *Nucl. Instruments Methods*  
708 *Phys. Res. Sect. A Accel. Spectrometers, Detect. Assoc. Equip.* 580 (2007) 442–445.  
709 doi:10.1016/j.nima.2007.05.073.
- 710 [31] S. Comas-Cardona, P. Le Grogne, C. Binetruy, P. Krawczak, Unidirectional compression of  
711 fibre reinforcements. Part 1: A non-linear elastic-plastic behaviour, *Compos. Sci. Technol.* 67  
712 (2007) 507–514. doi:10.1016/j.compscitech.2006.08.017.
- 713 [32] Q. Govignon, S. Bickerton, P.A. Kelly, Simulation of the reinforcement compaction and resin  
714 flow during the complete resin infusion process, *Compos. Part A Appl. Sci. Manuf.* 41 (2010)  
715 45–57. doi:10.1016/j.compositesa.2009.07.007.
- 716 [33] B. Yenilmez, E.M. Sozer, Compaction of e-glass fabric preforms in the Vacuum Infusion Process,  
717 A: Characterization experiments, *Compos. Part A Appl. Sci. Manuf.* 40 (2009) 499–510.  
718 doi:10.1016/j.compositesa.2009.01.016.
- 719 [34] Y. Wang, Y. Miao, D. Swenson, B.A. Cheeseman, C.-F. Yen, B. LaMattina, Digital element  
720 approach for simulating impact and penetration of textiles, *Int. J. Impact Eng.* 37 (2010) 552–560.  
721 doi:10.1016/j.ijimpeng.2009.10.009.
- 722 [35] Y. Miao, E. Zhou, Y. Wang, B.A. Cheeseman, Mechanics of textile composites: Micro-geometry,  
723 *Compos. Sci. Technol.* 68 (2008) 1671–1678. doi:10.1016/j.compscitech.2008.02.018.
- 724 [36] B. Cornelissen, R. Akkerman, Analysis of yarn bending behaviour, in: 17th Int. Conf. Compos.

725 Mater. (ICCM 17) , The British Composites Society, 2009.  
726 [37] H. Alshahrani, M. Hojjati, A new test method for the characterization of the bending behavior of  
727 textile prepregs, Compos. Part A Appl. Sci. Manuf. 97 (2017) 128–140.  
728 doi:10.1016/j.compositesa.2017.02.027.  
729